Received: 10 April 2024 | Revised: 6 May 2024 | Accepted: 8 May 2024

DOI: 10.1002/msd2.12109

RESEARCH ARTICLE

IJMSD International Journal of Mechanical System Dynamics Open Access WILEY

Boundary integrated neural networks and code for acoustic radiation and scattering

Wenzhen Qu[1] | Yan Gu[1] | Shengdong Zhao[1] | Fajie Wang[2] | Ji Lin[3]

[1]School of Mathematics and Statistics, Qingdao University, Qingdao, China

[2]College of Mechanical and Electrical Engineering, Qingdao University, Qingdao, China

[3]College of Mechanics and Materials, Hohai University, Nanjing, China

Correspondence
Prof. Yan Gu, School of Mathematics and Statistics, Qingdao University, Qingdao 266071, China.
Email: guyan1913@163.com

Funding information
Natural Science Foundation of Shandong Province of China, Grant/Award Numbers: ZR2022YQ06, ZR2021JQ02; Development Plan of Youth Innovation Team in Colleges and Universities of Shandong Province, Grant/Award Number: 2022KJ140; National Natural Science Foundation of China, Grant/Award Number: 12372199; Fund of the Key Laboratory of Road Construction Technology and Equipment, Chang'an University, Grant/Award Number: 300102253502; Water Affairs Technology Project of Nanjing, Grant/Award Number: 202203

Abstract

This paper presents a novel approach called the boundary integrated neural networks (BINNs) for analyzing acoustic radiation and scattering. The method introduces fundamental solutions of the time-harmonic wave equation to encode the boundary integral equations (BIEs) within the neural networks, replacing the conventional use of the governing equation in physics-informed neural networks (PINNs). This approach offers several advantages. First, the input data for the neural networks in the BINNs only require the coordinates of "boundary" collocation points, making it highly suitable for analyzing acoustic fields in unbounded domains. Second, the loss function of the BINNs is not a composite form and has a fast convergence. Third, the BINNs achieve comparable precision to the PINNs using fewer collocation points and hidden layers/neurons. Finally, the semianalytic characteristic of the BIEs contributes to the higher precision of the BINNs. Numerical examples are presented to demonstrate the performance of the proposed method, and a MATLAB code implementation is provided as supplementary material.

KEYWORDS

acoustic, semianalytical, physics-informed neural networks, boundary integral equations, boundary integral neural networks, unbounded domain

1 | INTRODUCTION

The boundary element method (BEM) has gained recognition as a formidable technique for numerically analyzing acoustic fields, owing to its semianalytical nature and boundary-only discretization.[1,2] By incorporating fundamental solutions into the BEM, the time-harmonic wave equation for acoustic problems, along with boundary conditions and the Sommerfeld radiation condition at infinity, can be transformed into boundary integral equations (BIEs).[3] Consequently, the BEM offers several advantages, including the reduction of problem dimensionality by one and the direct solution of unbounded domain problems without the need for special treatments.

Over the past decade, significant attention has been directed toward machine learning, owing to the remarkable advancements in computing resources and the abundance of available data.[4] Among the prominent tools in machine learning, deep neural networks (DNNs) have emerged as outstanding approximations of functions, demonstrating immense potential for numerical simulations of partial differential equation (PDE) problems.[5,6] Up to now, numerous DNN-based approaches have been devised to tackle PDEs, including physics-informed neural networks (PINNs),[7–9] the deep Galerkin method (DGM),[10,11] and the deep Ritz method (DRM).[12,13] The aforementioned DNN-based methods directly approximate the solution of problems using a neural network. Subsequently, a loss function or composite form is constructed, incorporating information from the residuals of the PDE with boundary/initial conditions or the energy functional form.

There have been remarkable contributions in acoustic numerical analysis through the utilization of DNN-based methods.[14,15] The DNNs are typically trained and applied in finite domains, which poses challenges when directly using them to solve unbounded domain problems. Very recently, Lin et al.[16] made the first attempt to integrate neural networks with indirect BIEs for solving PDE problems with Dirichlet boundary conditions. Following this, Zhang et al.[17] utilized neural networks to approximate solutions of direct BIEs using nonuniform rational B-splines (NURBS) parameterization of the boundary for potential problems. The aforementioned approaches are theoretically well-suited for addressing problems in unbounded domains. However, they have not been empirically validated by related problems in the references mentioned. Sun et al.[18] combined the neural networks with the BIEs to tackle potential and elastostatic problems, especially for cases with infinite/semi-infinite regions.

In this paper, we propose a novel approach called the boundary integrated neural networks (BINNs) to analyze acoustic problems in both bounded and unbounded domains. The method involves the approximated solutions of neural networks, trained solely on boundary collocation points, into the direct acoustic BIEs using quadratic elements. The loss function is then constructed based on the BIE residuals and is minimized specifically at these collocation points. Three numerical examples with various types of boundary conditions are provided to validate the proposed method. The numerical results obtained using the developed approach are compared with those obtained using the PINNs and the exact solutions.

2 | MATHEMATICAL FORMULATION FOR ACOUSTIC PROBLEM

The time-harmonic wave equation,[19] commonly referred to as the Helmholtz equation, can be expressed in two-dimensional (2D) domain Ω as follows:

$$\nabla^2 p(\mathbf{x}) + k^2 p(\mathbf{x}) = 0,\ \mathbf{x} \in \Omega, \tag{1}$$

where p represents the complex acoustic pressure, while k denotes the wave number. The wave number, defined as ω/c, corresponds to the ratio of the angular frequency ω to the speed of the acoustic wave c in the medium Ω. Equation (1) is subject to Dirichlet and Neumann boundary conditions (BCs) as

$$p(\mathbf{x}) = \bar{p}(\mathbf{x}),\quad \mathbf{x} \in \Gamma_D, \tag{2}$$

$$q(\mathbf{x}) = \frac{\partial \bar{p}(\mathbf{x})}{\partial \mathbf{n}(\mathbf{x})} = \mathrm{i}\rho\omega\bar{v}(\mathbf{x}), \mathbf{x} \in \Gamma_N, \tag{3}$$

where $\mathbf{n}(\mathbf{x})$ represents the outward unit normal vector to the boundary Γ at point x, ρ denotes the density of the medium, i means the imaginary unit, $\bar{v}(\mathbf{x})$ is the normal velocity, and the upper bars on the pressure and normal velocity indicate the known functions. Furthermore, as the distance r from the source tends to infinity, it is essential for the pressure field to satisfy the Sommerfeld radiation condition[20,21] as

$$\lim_{r\to\infty} \sqrt{r}\left(\frac{\partial p(r)}{\partial r} - \mathrm{i}kp(r)\right) = 0. \tag{4}$$

3 | BINNS

3.1 | BIEs

By incorporating the fundamental solutions, the time-harmonic wave equation for acoustic pressure can be transformed into an integral form[3] represented as

$$p(\mathbf{x}) + \int_\Gamma F(\mathbf{x},\mathbf{y})p(\mathbf{y})\mathrm{d}\Gamma(\mathbf{y}) = \int_\Gamma G(\mathbf{x},\mathbf{y})q(\mathbf{y})\mathrm{d}\Gamma(\mathbf{y}),\ \mathbf{x} \in \Omega, \tag{5}$$

where $\mathbf{x}$ and $\mathbf{y}$ represent the source and field points, respectively, while $G(\mathbf{x},\mathbf{y})$ and $F(\mathbf{x},\mathbf{y})$, respectively, denote the fundamental solutions of the time-harmonic wave equation and its corresponding normal derivatives, $q(\mathbf{y})$ is the normal derivative of acoustic pressure $p(\mathbf{y})$. $G(\mathbf{x},\mathbf{y})$, and $F(\mathbf{x},\mathbf{y})$ for 2D problems are defined as

$$G(\mathbf{x},\mathbf{y}) = \frac{\mathrm{i}}{4}H_0^{(1)}(kr(\mathbf{x},\mathbf{y})), \text{ and } F(\mathbf{x},\mathbf{y}) = \frac{\partial G(\mathbf{x},\mathbf{y})}{\partial n(\mathbf{y})}, \tag{6}$$

where $H_0^{(1)}$ represents the first kind Hankel function of order zero, r is the distance between points $\mathbf{x}$ and $\mathbf{y}$. Taking the limit as $\mathbf{x}$ in Equation (5) approaches the boundary Γ, we obtain

$$C(\mathbf{x})p(\mathbf{x}) + \int_\Gamma^{\mathrm{CPV}} F(\mathbf{x},\mathbf{y})p(\mathbf{y})\mathrm{d}\Gamma(\mathbf{y}) = \int_\Gamma G(\mathbf{x},\mathbf{y})q(\mathbf{y})\mathrm{d}\Gamma(\mathbf{y}),\quad \mathbf{x} \in \Omega, \tag{7}$$

in which $C(\mathbf{x}) = 0.5$ as the boundary near point $\mathbf{x}$ is smooth, and $\int_\Gamma^{\mathrm{CPV}}$ denotes the integral evaluated in the sense of Cauchy principal value (CPV). In this study, regular integrals are computed using the standard Gaussian quadrature with 20 Gaussian points, while the singular integrals are evaluated using a direct method developed by Guiggiani and Casalini[22] for CPV integrals. Also, BIEs need to treat the nearly singular integrals when calculating the physical quantities near the boundary. It is widely acknowledged that the handling techniques for singular and nearly singular integrals in BIEs have reached a high level of maturity. However, the detailed methods for handling these special integrals are beyond the scope of this work. Interested readers are referred to relevant Ref. 23–25 for further information.

3.2 | Discretization of BIEs

We discretize the BIEs using discontinuous quadratic element.[26] The shape functions, denoted as $N_i(\xi)(i = 1, 2, 3)$, of the elements are assumed to have the following forms:

$$N_1(\xi) = \frac{\xi(\xi-1)}{2}, N_2(\xi) = (1-\xi)(1+\xi), \text{ and } N_3(\xi) = \frac{\xi(\xi+1)}{2}, \tag{8}$$

in which $\xi \in [-1, 1]$ indicates the dimensionless coordinate. Then, the geometry of each quadratic element can be described as

$$\boldsymbol{y} = N_1(\xi)\boldsymbol{y}_1 + N_2(\xi)\boldsymbol{y}_2 + N_3(\xi)\boldsymbol{y}_3, \tag{9}$$

where $\boldsymbol{y}_1(\xi = -1)$, $\boldsymbol{y}_2(\xi = 0)$, and $\boldsymbol{y}_3(\xi = 1)$ denote the right, middle, and left points of the mentioned boundary element as shown in Figure 1, respectively. The pressure and its normal derivative on the boundary element are approximated by quantities $p_i, q_i (i = 1, 2, 3)$ on points $\boldsymbol{y}'_1(\xi = -\alpha)$, $\boldsymbol{y}'_2(\xi = 0)$, and $\boldsymbol{y}'_3(\xi = \alpha)$ in Figure 1, expressed as follows:

$$p(\boldsymbol{y}) = N_1\left(\frac{\xi}{\alpha}\right)p_1 + N_2\left(\frac{\xi}{\alpha}\right)p_2 + N_3\left(\frac{\xi}{\alpha}\right)p_3, \tag{10}$$

$$q(\boldsymbol{y}) = N_1\left(\frac{\xi}{\alpha}\right)q_1 + N_2\left(\frac{\xi}{\alpha}\right)q_2 + N_3\left(\frac{\xi}{\alpha}\right)q_3, \tag{11}$$

where $\alpha \in (0, 1)$. In the numerical calculations of this work, the value of α is set to 0.8. It should be noted that the parameter α in Equation (10) or Equation (11) is free to choose a value from the range (0, 1), which has little influence on the numerical accuracy of the present method.

Based on the aforementioned discontinuous quadratic element, the discretized form of the BIE (7) is given as

$$\begin{aligned} C(\boldsymbol{x}^m)p(\boldsymbol{x}^m) &+ \sum_{i=1}^{N}\sum_{j=1}^{3} p_j^i \int_{-1}^{1} F(\boldsymbol{x}^m, \boldsymbol{y}_i(\xi))N_j(\xi/\alpha)J_i(\xi)d\xi \\ &= \sum_{i=1}^{N}\sum_{j=1}^{3} q_j^i \int_{-1}^{1} G(\boldsymbol{x}^m, \boldsymbol{y}_i(\xi))N_j(\xi/\alpha)J_i(\xi)d\xi, \end{aligned} \tag{12}$$

where N represents the number of boundary elements, $\boldsymbol{x}^m(m = 1, 2, ..., 3N)$ are boundary collocation points and selected to be the same set as points $\boldsymbol{y}'_j$ (see Figure 1) on these elements, p_j^i and q_j^i, respectively, denote the pressure and its normal derivative at the jth collocation point of the ith element, and $J_i(\xi)$ represents the Jacobian of transformation from the global coordinate $\boldsymbol{y}$ to the dimensionless coordinate ξ for integrals at the ith element.

After discretizing the BIEs through the process mentioned earlier, we can define the following two functions with Equation (12) to facilitate the construction of the loss function in subsequent steps

$$\begin{aligned} LE(\boldsymbol{x}^m, \boldsymbol{p}) = C(\boldsymbol{x}^m)p(\boldsymbol{x}^m) &+ \sum_{i=1}^{N}\sum_{j=1}^{3} p_j^i \int_{-1}^{1} \\ &F(\boldsymbol{x}^m, \boldsymbol{y}_i(\xi))N_j(\xi/\alpha)J_i(\xi)d\xi, \end{aligned} \tag{13}$$

$$RE(\boldsymbol{x}^m, \boldsymbol{q}) = \sum_{i=1}^{N}\sum_{j=1}^{3} q_j^i \int_{-1}^{1} G(\boldsymbol{x}^m, \boldsymbol{y}_i(\xi))N_j(\xi/\alpha)J_i(\xi)d\xi, \tag{14}$$

where $\boldsymbol{p} = \left\{p_j^i\right\}_{j=1,2,3}^{i=1,...,N}$ and $\boldsymbol{q} = \left\{q_j^i\right\}_{j=1,2,3}^{i=1,...,N}$.

3.3 | Neural networks and loss function of the BINNs

We present the construction of the BINNs by seamlessly integrating neural networks and the BIEs in this section. As illustrated in Figure 2, we utilize a fully connected neural architecture including the input layer, the L hidden layers, and the output layer. The number of neurons in l hidden layer is set to n_l. Based on the neural networks approximation, the real and imaginary parts of trial solutions of pressures at a collocation point $\boldsymbol{x}$ can be expressed as

$$\mathrm{Re}\{p(\boldsymbol{x}, \boldsymbol{w}, \boldsymbol{b})\} = \hbar_1(\lambda_L(\lambda_{L-1}(...(\lambda_1(\boldsymbol{x}))))), \tag{15}$$

$$\mathrm{Im}\{p(\boldsymbol{x}, \boldsymbol{w}, \boldsymbol{b})\} = \hbar_2(\lambda_L(\lambda_{L-1}(...(\lambda_1(\boldsymbol{x}))))), \tag{16}$$

where $\hbar_k(k = 1, 2)$ and $\lambda_l(l = 1, 2, ..., L)$ are linear and nonlinear mappings, expressed as follows

$$\hbar_k(g) = \boldsymbol{w}'_k * g + b'_k, \tag{17}$$

$$\lambda_l(g) = \sigma(\boldsymbol{w}_l * g + \boldsymbol{b}_l), \tag{18}$$

with weights $\boldsymbol{w}'_k \in R^{n_L}$, $\boldsymbol{w}'_l \in R^{n_l * n_{l-1}}(n_0 = 2)$, biases $b'_k \in R$, $\boldsymbol{b}'_l \in R^{n_l}$, and the activation function σ. Here, Table 1 lists some commonly used activation functions. To obtain the normal derivatives of acoustic pressures approximated by the above neural networks, we employ the "dlgradient," which is an automatic differentiation function in the Deep Learning Toolbox of MATLAB. Additionally, complex acoustic pressure is not directly approximated using a neural network due to limitations of some functions in the Deep Learning Toolbox, which does not support computations involving complex numbers.

We construct two different forms of loss functions and will explore their performance in the next sections. First, we incorporate the known pressures p and/or normal derivatives q directly into the BIEs, creating the following loss function referred to as *Loss*

$$Loss = \frac{1}{3N}\sum_{m=1}^{3N}(LE(\boldsymbol{x}^m, \boldsymbol{p}) - RE(\boldsymbol{x}^m, \boldsymbol{q}))^2, \tag{19}$$

where the unknown p and/or q on the boundary are approximated by the neural networks. For the second form of the loss function, we approximate both the pressures and normal derivatives in the BIEs

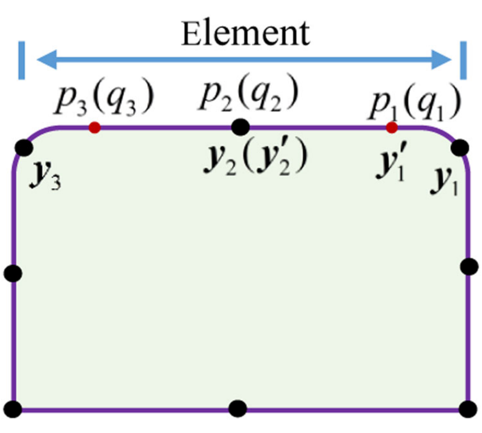

FIGURE 1 Discontinuous quadratic element.

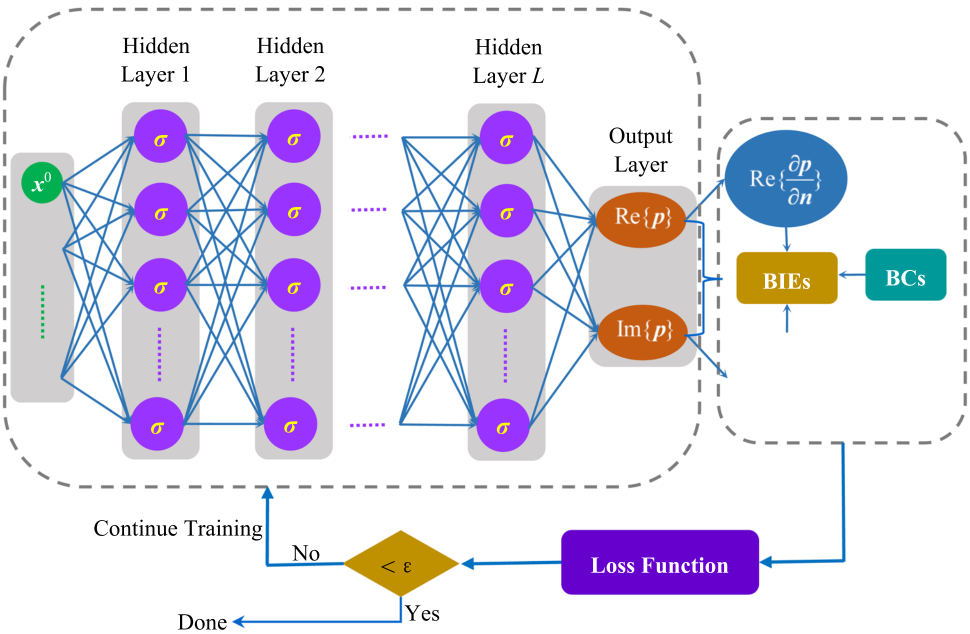

FIGURE 2 The framework of the boundary integrated neural networks.

TABLE 1 Some commonly used activation functions.

	Arctan	Sigmoid	Swish	Softplus	Tanh
$\sigma(z)$	$\arctan(z)$	$\frac{1}{1+e^{-z}}$	$\frac{z}{1+e^{-z}}$	$\ln(1+e^{z})$	$\frac{e^{z}-e^{-z}}{e^{z}+e^{-z}}$
	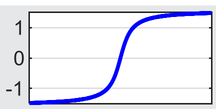	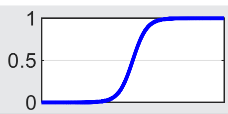	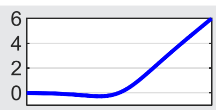	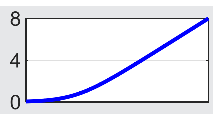	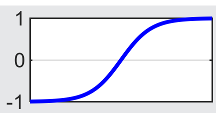

and boundary constraints using the neural networks. The loss function named as Loss $Loss_{BC}$ is then constructed as

$$Loss_{BC}=\frac{1}{3N}\sum_{m=1}^{3N}(LE(\mathbf{x}^m,\mathbf{p})-RE(\mathbf{x}^m,\mathbf{q}))^2+\frac{1}{N_D}\sum_{m=1}^{N_D}(p_D-\bar{p}_D)^2+\frac{1}{N_N}\sum_{m=1}^{N_N}(q_N-\bar{q}_N)^2, \tag{20}$$

where the subscripts D and N, respectively, denote the Dirichlet and the Neumann BC, N_D and N_N indicate the numbers of Dirichlet and Neumann boundary collocation points, respectively, and the superscript bar represents the known quantities. It should be noted that the BINNs are developed based on the BIEs and thus are unsuitable for numerical simulations of problems without fundamental solutions.

3.4 | Optimization of parameters and solution of pressure at interior point

In the previous sections, we have established the architecture of the neural networks and defined the loss function for the BINNs. The next step is to optimize the weights and biases of each neuron by minimizing the corresponding loss function, either Equation (19) or Equation (20). To accomplish this optimization process, we utilize the powerful and widely used "fmincon" function in MATLAB. The "fmincon" is specifically designed to minimize constrained nonlinear multivariable functions.

By applying this optimization approach, we are able to obtain accurate numerical results for the unknown pressures and normal derivatives along the boundary. Once the pressures p and normal derivatives q at the boundary collocation points are determined, we can easily calculate the numerical solution for the pressure at any interior point using Equation (5).

4 | NUMERICAL EXAMPLES

To evaluate the performance of the BINNs, several benchmark examples involving bounded and unbounded domains under various BCs are provided. The accuracy of the present approach is thoroughly investigated by examining the influence of parameters such as the hidden layer number, neuron number in each layer, and the choice of activation function. The numerical results calculated by the BINNs are compared against those obtained using the traditional PINNs as well as the theoretical solutions.

All the MATLAB codes used in this study are executed on a computer equipped with an Intel Core i9-11900F 2.5 GHz CPU and 64 GB of memory. The precision of the numerical results is assessed using relative error, which is defined as[27]

$$\text{Relative error (RE)} = \sqrt{\sum_{i=1}^{M}(\tilde{p}_i - p_i)^2} \Big/ \sqrt{\sum_{i=1}^{M} p_i^{\,2}}, \tag{21}$$

where M denotes the number of calculated points, and $\tilde{p}_i$ and p_i are numerical and analytical solutions at ith calculated point, respectively.

4.1 | Interior acoustic field

As the first example, we consider the distribution of acoustic pressure in a rectangle domain with a length of 3 m and a height of 1.5 m, as illustrated in Figure 3. The center of the domain is (1.5, 0.75). The boundary is subject to two different cases of BCs.

Case 1: Dirichlet BC.

The pressure on the boundary is specified as

$$p(x_1', x_2') = \cos(kx_1') + \mathrm{i}\sin(kx_2'),\ \ (x_1', x_2') \in \Gamma. \tag{22}$$

Obviously, the analytical solution for this case is $p(x_1, x_2) = \cos(kx_1) + \mathrm{i}\sin(kx_2),\ (x_1, x_2) \in \Omega$.

Initially, we assess the performance of the BINNs using two distinct forms of loss functions. Four distinct neural architectures are configured as follows: (a) a single hidden layer consisting of 10 neurons; (b) a single hidden layer consisting of 20 neurons; (c) two hidden layers, each with 10 neurons; and (d) two hidden layers, each with 20 neurons. The training process for optimization stops when the iteration count reaches 10 000. A total of 270 boundary collocation points, corresponding to 90 boundary elements, are utilized. The activation function selected for neural networks is $\sigma(z) = z/(1 + e^{-z})$. The wave number is set to $k = 2\,\text{m}^{-1}$.

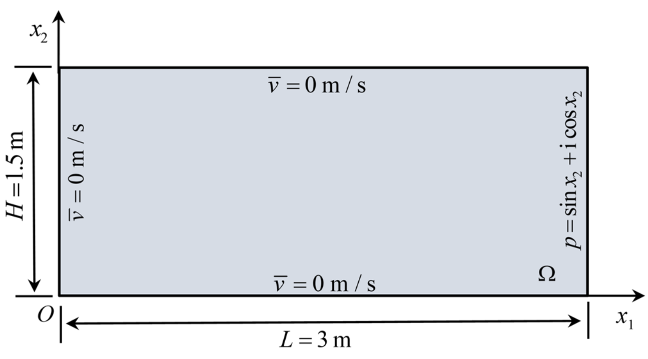

FIGURE 3 The dimension of the rectangle domain and the BCs of case 2.

Using the BINNs with *Loss* and $Loss_{BC}$, Table 2 presents the relative errors of the real and imaginary components of the pressure along the evaluated line $x_2 = 0.75$ m with 30 equally spaced points for calculation purposes. The numerical results obtained through the use of *Loss* showcase superior accuracy when compared to the results obtained using $Loss_{BC}$. Remarkably, even using the networks with a single hidden layer consisting of 10 neurons, the present method with *Loss* achieves high accuracy in the numerical results. Additionally, there is a slight improvement when employing more hidden layers or increasing the number of neurons in each layer. In contrast, the BINNs with $Loss_{BC}$ require a greater number of hidden layers and neurons to attain sufficiently accurate results.

Figure 4 illustrates the convergence process of two designated loss functions *Loss* and $Loss_{BC}$ over iterations ranging from 1 to 10 000, with values recorded at every 100 iterations. It is apparent that *Loss* exhibits a faster convergence rate compared to $Loss_{BC}$. Therefore, the BINNs with *Loss* have a better performance in comparison to that with $Loss_{BC}$, as indicated in Table 2. To expedite the convergence process of the loss function $Loss_{BC}$, the incorporation of additional learning techniques is necessary to balance its different loss terms. Consequently, *Loss* stands as the superior choice for an efficient loss function in the context of BINNs when compared to $Loss_{BC}$. Henceforth, the BINNs will employ *Loss* in all subsequent computational processes unless otherwise specified.

Next, we present a comparison of the accuracy of the numerical results obtained using the BINNs and the traditional PINNs. The same calculated points are distributed on the line $x_2 = 0.75$ m. The wave number, activation functions of the neural networks, and optimization stopping criteria for both methods remain consistent with the previous settings. The BINNs adopt a single hidden layer comprising 20 neurons, while the PINNs utilize two different networks: (a) a single hidden layer with 20 neurons, and (b) three hidden layers, each containing 20 neurons. The collocation points for the PINNs are uniformly distributed within the rectangular domain and its boundary, while for the BINNs, they are only placed on the boundary. Figures 5 and 6 plot the convergence curves of the pressures obtained by the BINNs and the PINNs as the number of collocation points increases.

TABLE 2 Errors of pressures by the BINNs based on four neural networks.

	Loss				$Loss_{BC}$			
Error	**a**	**b**	**c**	**d**	**a**	**b**	**c**	**d**
Re{p}	2.38E−06	4.66E−07	5.74E−07	1.38E−07	2.07E−02	2.77E−03	4.09E−05	3.85E−05
Im{p}	6.43E−07	7.30E−08	2.88E−07	9.12E−08	3.61E−03	7.41E−04	8.96E−05	5.62E−05

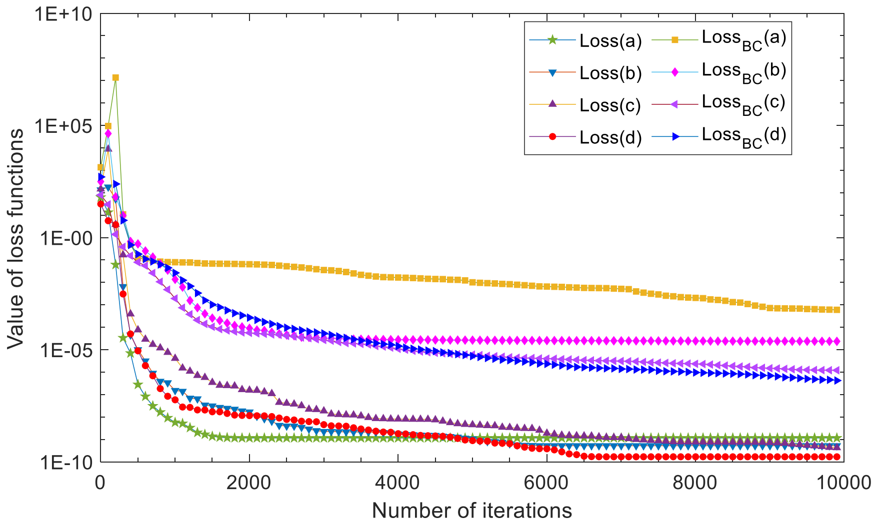

FIGURE 4 Convergence process of loss functions constructed with different neural architectures.

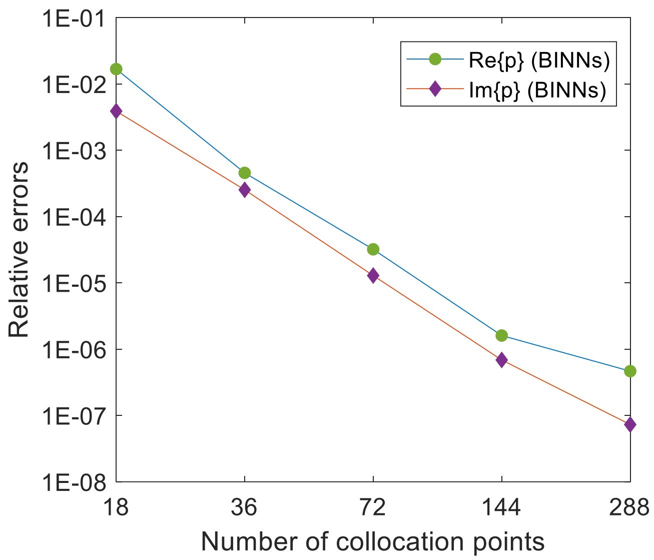

FIGURE 5 Convergence curves of pressures by the boundary integrated neural networks (BINNs) with different number of collocation points.

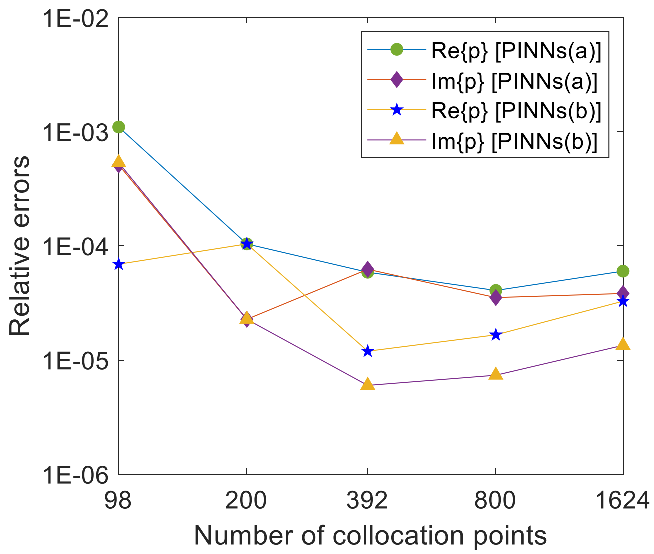

FIGURE 6 Convergence curves of pressures by the physics-informed neural networks (PINNs) with different number of collocation points.

Clearly, the BINNs exhibit a faster and more stable convergence rate compared to the PINNs with networks "a" or "b." Furthermore, the precision of the pressures evaluated by the BINNs is higher even with a smaller number of collocation points, as compared to the PINNs. Therefore, to achieve comparable precision in pressure calculations, the BINNs necessitate significantly fewer collocation points and hidden layers/neurons compared to the PINNs. This observation also demonstrates that the BINNs exhibit higher computational efficiency in comparison to the PINNs.

Case 2: Mixed BCs.

The mixed BCs are taken into account in this particular case. As depicted in Figure 3, the left, upper and lower boundaries of the domain are assumed to be rigid, while the right boundary is subjected to a specific condition as

$$p(3, x_2') = \sin x_2' + \mathrm{i}\cos x_2', (3, x_2') \in \Gamma. \tag{23}$$

The analytical solution for the case is not available.

The wave number is assumed to be $k = 2\,\mathrm{m}^{-1}$. Both the BINNs and the PINNs are employed for the numerical simulation of this case to make a comparison. The activation functions of the neural networks remain the same as in case 1, and the training process for optimization stops after 10 000 iterations. The BINNs use 288 collocation points and a single hidden layer with 20 neurons, while the PINNs use 1624 collocation points and three hidden layers, each with 25 neurons. Figure 7 displays the numerical results of the pressures in the entire computational domain. As observed from the figure, the numerical results obtained by the BINNs show good agreement with those calculated by the PINNs.

4.2 | Acoustic radiation of an infinite pulsating cylinder

The second example focuses on the analysis of acoustic radiation from an infinite pulsating cylinder. The cylinder has a radius of $R = 1\,\text{m}$, and its center is located at (0, 0). The boundary of the structure has a normal velocity amplitude of $\bar{v} = 1\,\text{m/s}$. The analytical solution for the pressure can be determined as

$$p(r) = \mathrm{i}\rho c\bar{v}\,\frac{H_0^1(kr)}{H_1^1(kR)},\quad r \geq R. \tag{24}$$

where $H_i^1\,(i = 0, 1)$ denotes the ith order Hankel function of the first kind. The medium for the propagation of acoustic waves is assumed to be air, with a density of $\rho = 1.2\,\text{kg/m}^3$ and a wave speed of $c = 341\,\text{m/s}$.

In this simulation, the wave number $k = 1\,\text{m}^{-1}$ is selected. The BINNs employ neural networks consisting of two hidden layers, each comprising 10 neurons. The training process for optimization terminates after 2000 iterations. The present approach utilizes 150 collocation points on the boundary. The chosen activation function is "Swish," as specified in Table 1. Calculated points are distributed within a domain $\{(x_1, x_2) \mid \sqrt{x_1^2 + x_2^2} > 1, -5 < x_1, x_2 < 5\}$. Figure 8 presents the contour plots of relative errors for the real and imaginary components of pressures at the calculated points, as evaluated by the BINNs. It is evident that the present approach yields satisfactory numerical results.

Maintaining the previous settings unaltered, we proceed to validate the impact of various activation functions listed in Table 1 on the developed method. Table 3 shows the numerical errors of pressures in domain $\{(x_1, x_2) \mid \sqrt{x_1^2 + x_2^2} > 1, -5 < x_1, x_2 < 5\}$, along with the CPU time and the final values of *Loss*, obtained using the BINNs with different activation functions. From the table, it indicates that the choice of activation functions has minimal effect on the precision, convergence process of the loss function, and the efficiency of the BINNs.

4.3 | Acoustic scattering of an infinite rigid cylinder

As the last numerical example, we consider an acoustic scattering phenomenon. A plane incident wave, with an amplitude of unity, travels along the positive x-axis and impinges on an infinite rigid cylinder centered at point (0, 0) with a radius of $R = 1\,\text{m}$. The analytical solution of scattering field

$$p(r,\theta) = -\sum_{n=0}^{\infty} \varepsilon_n \mathrm{i}^n \frac{J_n'(kR)}{H_n^{1\prime}(kR)} H_n^1(kr)\cos(n\theta),\quad r \geq R, \tag{25}$$

where J_n denotes the nth order Bessel function, H_n^1 represents the nth order Hankel function of the first kind, $\theta = 0$ along the positive x-axis, and ε_n is the Neumann symbol expressed as

$$\varepsilon_n = \begin{cases} = 1, n = 0, \\ = 2, n \geq 1. \end{cases} \tag{26}$$

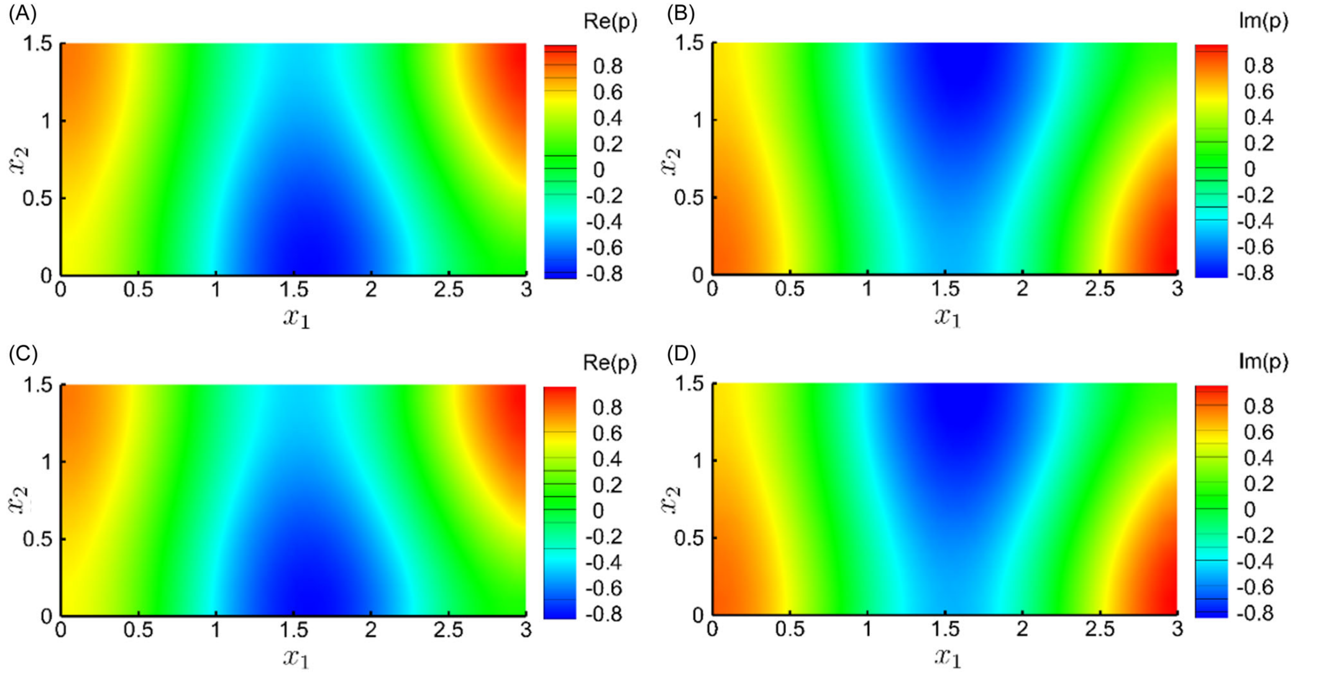

FIGURE 7 Numerical results of pressures in the rectangle domain: (A) real component (the BINNs); (B) imaginary component (the BINNs); (C) real component (the PINNs); (D) imaginary component (the PINNs). BINN, boundary integrated neural network; PINN, physics-informed neural network.

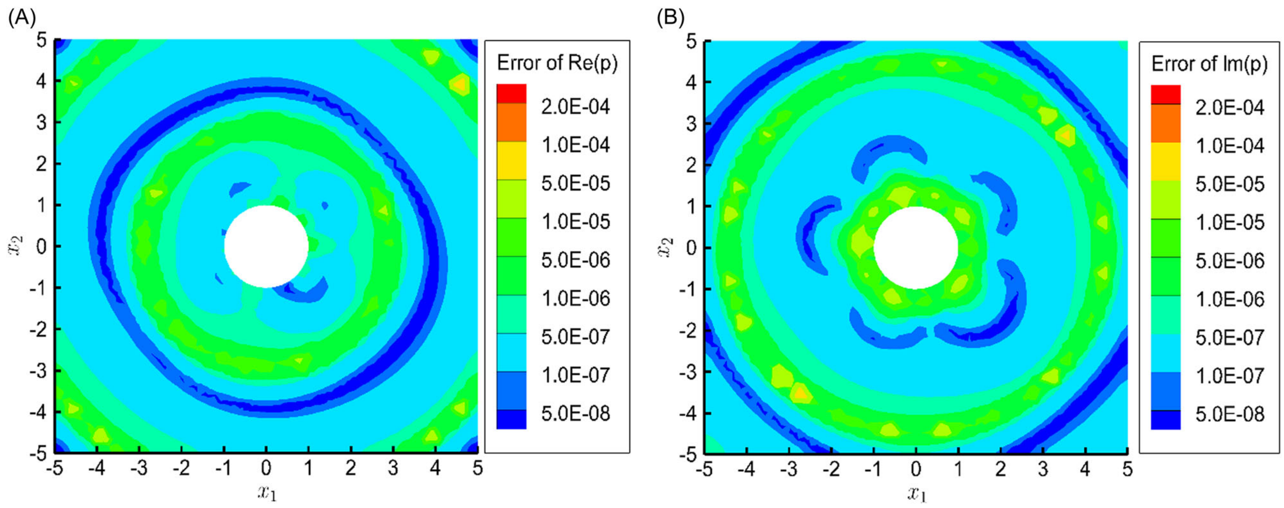

FIGURE 8 Numerical results of pressures calculated by the boundary integrated neural networks: (A) relative error of real component of pressure; (B) relative error of imaginary component of pressure.

TABLE 3 Impact of various activation functions on the BINNs.

Activation functions	Arctan	Sigmoid	Swish	Softplus	Tanh
Error of Re{p}	1.10E−06	5.44E−06	9.97E−07	4.59E−07	1.02E−06
Error of Im{p}	1.20E−06	6.72E−06	1.02E−06	6.67E−07	2.19E−06
Final value of *Loss*	7.15E−10	1.47E−09	4.87E−10	8.95E−11	2.95E−09
CPU time (s)	21.6	23.5	21.9	22.0	21.8

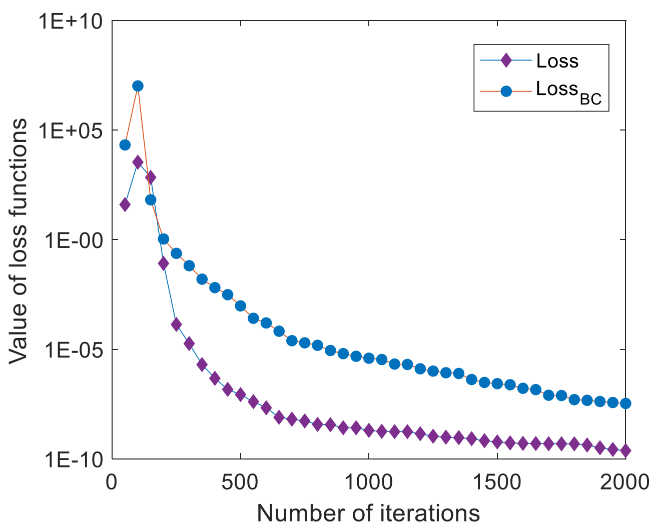

FIGURE 9 Convergence process of loss functions.

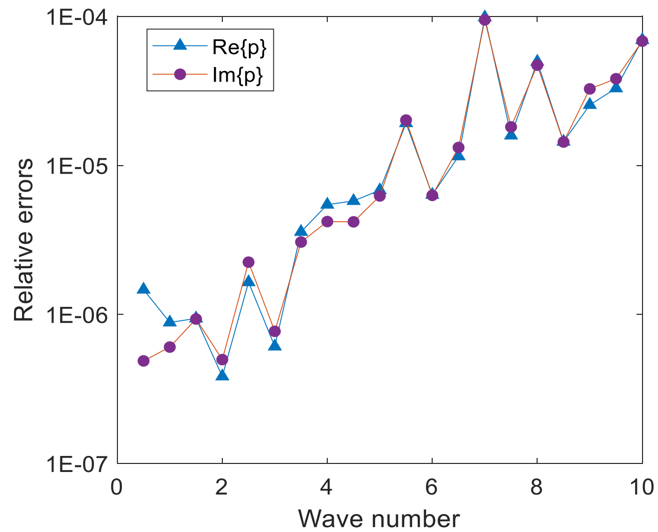

FIGURE 10 Variations of relative errors of pressures with different wave numbers.

A neural network with a configuration of two hidden layers, each consisting of 20 neurons, is utilized for the numerical implementation of the BINNs. The wave number is set to $k = 0.5\,\text{m}^{-1}$, and a total of 90 collocation points are distributed on the boundary. The activation function is set to $\sigma(z) = z/(1 + e^{-z})$. Two loss functions, specifically Equations (19) and (20), are reconsidered and incorporated into the BINNs for analyzing acoustic fields in unbounded domains. Figure 9 depicts the convergence behavior of two designated loss functions, namely *Loss* and $Loss_{BC}$, as the iterations progress from 1 to 2 000, with measurements taken every 50 iterations. Once again, it is demonstrated that *Loss* has a better convergence performance when compared to $Loss_{BC}$.

The number of collocation points on the boundary is adjusted to 300, and the training process for optimization is conducted over 5 000 iterations. All other settings remain unchanged from the previous

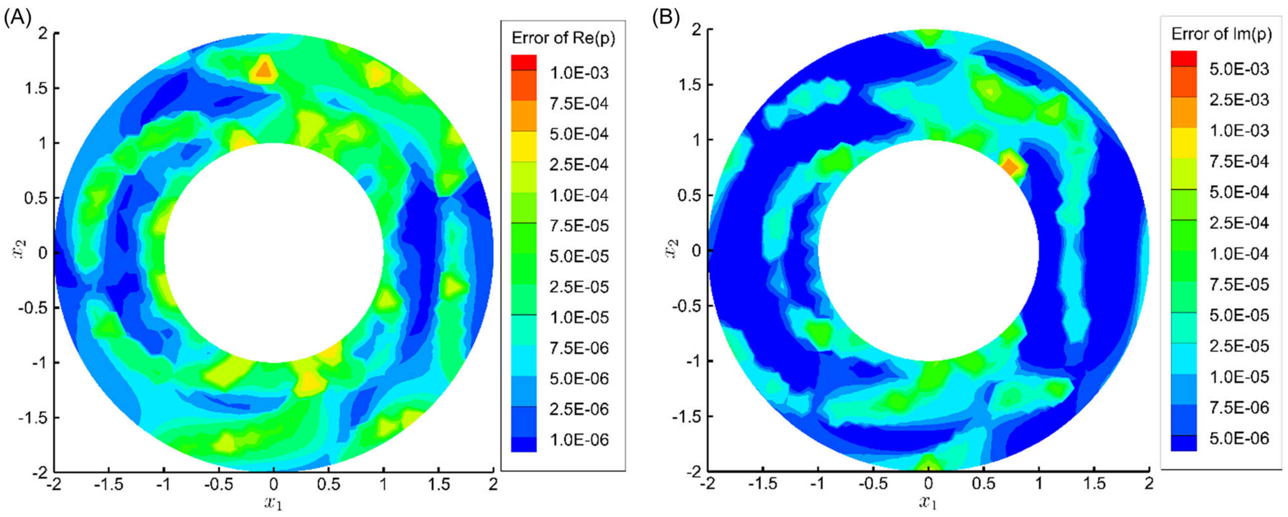

FIGURE 11 Numerical errors of pressures calculated by the BINNs for $k = 5\,\mathrm{m}^{-1}$: (A) relative error of real component of pressure; (B) relative error of imaginary component of pressure.

configuration. Employing the BINNs with *Loss*, Figure 10 displays the relative errors of pressures in domain $\{(x_1, x_2) \,|\, 1 < \sqrt{x_1^2 + x_2^2} < 2\}$ across varying wave numbers ranging from 0.5 to $10\,\mathrm{m}^{-1}$. As we can observe in Figure 10, the developed method obtains accurate numerical results for different wave numbers. Figure 11 presents the relative errors of pressures at all calculated points within domain $\{(x_1, x_2) \,|\, 1 < \sqrt{x_1^2 + x_2^2} < 2\}$, considering a wave number of $k = 5\,\mathrm{m}^{-1}$. It can be observed that maximum relative error of both the real and imaginary parts of pressures at these calculated points is below 5E−003.

These numerical results obtained using the BINNs further illustrate the competitiveness of the proposed method in simulating acoustic fields in unbounded domains, surpassing the traditional PINNs.

5 | CONCLUDING REMARKS

The BINNs is proposed in this paper as a numerical approach for analyzing acoustic fields in both bounded and unbounded domains. Unlike the traditional PINNs that combine the governing equation with neural architectures, the proposed method integrates the BIEs and neural networks. Through numerical experiments on various benchmark examples, the BINNs exhibit high accuracy and rapid convergence. Several notable advantages of the BINNs over the traditional PINNs in the context of acoustic radiation and scattering can be summarized as follows:

1) The BINNs only require the coordinates of "boundary" collocation points as input data for the neural networks. The benefit of this is that the method is particularly well-suited for numerical simulations of problems in unbounded domains.
2) The loss function in the BINNs, as defined in Equation (19), is not a composite form. Therefore, there is no need to consider special techniques to balance the influence between different terms, as described in Equation (20) or the loss function used in the PINNs. The numerical results also demonstrate the fast convergence of the loss function.
3) To achieve comparable precision in pressure calculations, the BINNs require significantly fewer collocation points and hidden layers/neurons compared to the PINNs. As a result, the BINNs exhibit higher computational efficiency.
4) The BINNs have higher precision attributed to the semianalytic characteristic of the BIEs, as evident from the numerical errors of acoustic pressures obtained using this method.

The present approach is introduced to address relatively simple acoustic problems, and several conclusions are summarized. In the future, we aim to extend the application of BINNs to structural-acoustic sensitivity analysis. In addition, when using the present method to solve high-frequency acoustic problems, high wave numbers may lead to issues such as loss function oscillation or gradient vanishing, making the optimization process challenging or even nonconvergent. We remain committed to exploring this intricate issue in our future research.

ACKNOWLEDGMENTS

The research presented in this paper received support from the Natural Science Foundation of Shandong Province of China (Grant Nos. ZR2022YQ06 and ZR2021JQ02), the Development Plan of Youth Innovation Team in Colleges and Universities of Shandong Province (Grant No. 2022KJ140), the National Natural Science Foundation of China (Grant No. 12372199), the Key Laboratory of Road Construction Technology and Equipment (Chang'an University, Grant No. 300102253502), and the Water Affairs Technology Project of Nanjing (Grant No. 202203).

CONFLICT OF INTEREST STATEMENT

The authors declare no conflict of interest.

DATA AVAILABILITY STATEMENT

The data that support the findings of this study are available from the corresponding authors upon reasonable request.

ORCID

Yan Gu http://orcid.org/0000-0002-8510-3193
Fajie Wang http://orcid.org/0000-0002-5162-1099

REFERENCES

1. Koo BU. Shape design sensitivity analysis of acoustic problems using a boundary element method. *Comput Struct*. 1997;65(5):713-719.
2. Zheng C, Matsumoto T, Takahashi T, Chen H. A wideband fast multipole boundary element method for three dimensional acoustic shape sensitivity analysis based on direct differentiation method. *Eng Anal Bound Elem*. 2012;36(3):361-371.
3. Chen L, Zheng C, Chen H. A wideband FMBEM for 2D acoustic design sensitivity analysis based on direct differentiation method. *Comput Mech*. 2013;52:631-648.
4. Jordan MI, Mitchell TM. Machine learning: trends, perspectives, and prospects. *Science*. 2015;349(6245):255-260.
5. Ruthotto L, Haber E. Deep neural networks motivated by partial differential equations. *J Math Imaging Vision*. 2020;62:352-364.
6. Zeng S, Zhang Z, Zou Q. Adaptive deep neural networks methods for high-dimensional partial differential equations. *J Comput Phys*. 2022;463:111232.
7. Raissi M, Perdikaris P, Karniadakis GE. Physics-informed neural networks: a deep learning framework for solving forward and inverse problems involving nonlinear partial differential equations. *J Comput Phys*. 2019;378:686-707.
8. Yang L, Meng X, Karniadakis GE. B-PINNs: Bayesian physics-informed neural networks for forward and inverse PDE problems with noisy data. *J Comput Phys*. 2021;425:109913.
9. Gu Y, Zhang C, Zhang P, Golub MV, Yu B. Enriched physics-informed neural networks for 2D in-plane crack analysis: theory and MATLAB code. *Int J Solids Struct*. 2023;276:112321.
10. Sirignano J, Spiliopoulos K. DGM: a deep learning algorithm for solving partial differential equations. *J Comput Phys*. 2018;375:1339-1364.
11. Saporito YF, Zhang Z. Path-dependent deep Galerkin method: a neural network approach to solve path-dependent partial differential equations. *SIAM J Financial Math*. 2021;12(3):912-940.
12. E W, Yu B. The deep Ritz method: a deep learning-based numerical algorithm for solving variational problems. *Commun Math Stat*. 2018;6(1):1-12.
13. Gu Y, Ng MK. Deep Ritz method for the spectral fractional laplacian equation using the Caffarelli–Silvestre extension. *SIAM J Scientific Comput*. 2022;44(4):A2018-A2036.
14. Song C, Alkhalifah T, Waheed UB. Solving the frequency-domain acoustic VTI wave equation using physics-informed neural networks. *Geophys J Int*. 2021;225(2):846-859.
15. Zhang Y, Zhu X, Gao J. Seismic inversion based on acoustic wave equations using physics-informed neural network. *IEEE Trans Geosci Remote Sensing*. 2023;61:1-11.
16. Lin G, Hu P, Chen F, et al. BINet: learn to solve partial differential equations with boundary integral networks. *CSIAM Trans Appl Math*. 2023;4:275-305.
17. Zhang H, Anitescu C, Bordas S, Rabczuk T, Atroshchenko E. Artificial neural network methods for boundary integral equations. TechRxiv Preprint techrxiv20164769v1. 2022.
18. Sun J, Liu Y, Wang Y, Yao Z, Zheng X. BINN: a deep learning approach for computational mechanics problems based on boundary integral equations. *Comput Methods Appl Mech Eng*. 2023;410:116012.
19. Qu W, Zheng C, Zhang Y, Gu Y, Wang F. A wideband fast multipole accelerated singular boundary method for three-dimensional acoustic problems. *Comput Struct*. 2018;206:82-89.
20. Schot SH. Eighty years of Sommerfeld's radiation condition. *Historia Math*. 1992;19:385-401.
21. Qu W, Chen W, Zheng C. Diagonal form fast multipole singular boundary method applied to the solution of high-frequency acoustic radiation and scattering. *Int J Numer Meth Eng*. 2017;111:803-815.
22. Guiggiani M, Casalini P. Direct computation of Cauchy principal value integrals in advanced boundary elements. *Int J Numer Meth Eng*. 1987;24(9):1711-1720.
23. Zhang Y. Evaluation of singular and nearly singular integrals in the BEM with exact geometrical representation. *J Computat Math*. 2013;31:355-369.
24. Xie G, Zhou F, Li H, Wen X, Meng F. A family of non-conforming crack front elements of quadrilateral and triangular types for 3D crack problems using the boundary element method. *Front Mech Eng*. 2019;14:332-341.
25. Xie G, Zhang D, Meng F, Du W, Zhang J. Calculation of stress intensity factor along the 3D crack front by dual BIE with new crack front elements. *Acta Mech*. 2017;228:3135-3153.
26. Qu W, Chen W, Fu Z. Solutions of 2D and 3D non-homogeneous potential problems by using a boundary element-collocation method. *Eng Anal Bound Elem*. 2015;60:2-9.
27. Qu W, Gu Y, Fan CM. A stable numerical framework for long-time dynamic crack analysis. *Int J Solids Struct*. 2024;293:112768.

AUTHOR BIOGRAPHIES

Wenzhen Qu received his doctoral degree in engineering mechanics from Hohai University in 2016 and is now an associate professor in the College of Mathematics and Statistics at Qingdao University, China. He has authored or coauthored more than 60 publications in journals. His research activities include computational mechanics, computational wave propagation, machine learning, and fracture and damage mechanics.

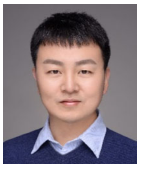

Yan Gu received a PhD from Hohai University in 2014 and is now a professor in the College of Mathematics and Statistics at Qingdao University. His research activities include computational mechanics, fracture and damage mechanics, hydrodynamics, acoustics, and applied inverse problems. He has been awarded the Humboldt Research Fellowship for Postdoctoral Researchers, the ICACM Young Investigator Award for Promising Research on Novel Computational Methods, and the DU Qing-Hua Medal of Computational Methods in Engineering.

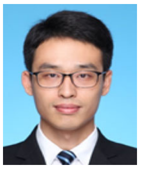

Shengdong Zhao obtained his doctoral degree in 2018 from Beijing Jiaotong University. He is currently employed as an associate professor at the School of Mathematics and Statistics, Qingdao University. He has been engaged in research in the fields of finite element computation, topological optimization design, differential equation modeling and solving, acoustical metamaterial design, underwater acoustics detection, and stealth design.

Fajie Wang received a PhD degree in fluid mechanics from Hohai University, Nanjing, China, in 2018. He is currently a professor at the College of Mechanical and Electrical Engineering, Qingdao University, China. He has authored or coauthored more than 80 publications in journals. His research interests include computational mechanics, machine learning, optimum structural design, and fractal and fractional modeling.

Ji Lin received his doctoral degree in engineering mechanics from Hohai University in 2014 and has been a professor at Hohai University, China. Currently, he is serving as a member of the committee of several provincial and international scientific societies. Prof. Lin's research activities include computational mechanics, computational mathematics, software development, and so forth. His overall research output has culminated in more than 100 publications and one book in internationally respected journals, which have been cited more than 2 200 times by researchers. Among them, seven papers have been selected as ESI highly cited papers. He is the PI of two projects funded by the NSFC and has conducted more than 15 provincial projects.

How to cite this article: Qu W, Gu Y, Zhao S, Wang F, Lin J. Boundary integrated neural networks and code for acoustic radiation and scattering. *Int J Mech Syst Dyn*. 2024;4:131-141. doi:10.1002/msd2.12109